# Pre-doped Cations in $V_2O_5$ for High-performance Zn-ion Batteries

Yinan Lu,[1] Tianlei Wang,[2] Joanna Borowiec,[2] Ivan P. Parkin,[2,*] Buddha Deka Boruah[1,*]

[1]Institute for Materials Discovery, University College London, London WC1E 7JE, Kingdom United

[2]Department of Chemistry, University College London, London WC1H 0AJ, United Kingdom

*Corresponding authors: Prof. Ivan P. Parkin – i.p.parkin@ucl.ac.uk

Dr. Buddha Deka Boruah – b.boruah@ucl.ac.uk

**Abstract**

Aqueous rechargeable zinc-ion batteries (ZIBs) have garnered considerable attention due to their safety, cost-effectiveness, and eco-friendliness. There is a growing interest in finding suitable cathode materials for ZIBs. Layered vanadium oxide has emerged as a promising option due to its ability to store zinc ions with high capacity. However, the advancement of high-performance ZIBs encounters obstacles such as sluggish diffusion of zinc ions resulting from the high energy barrier between $V_2O_5$ layers, degradation of electrode structure over time and consequently lower capacity than the theoretical value. In this study, we investigated the pre-doping of different cations (including $Na^+$, $K^+$, and $NH_4^+$) into $V_2O_5$ to enhance the overall charge storage performance. Our findings indicate that the presence of $V^{4+}$ enhances the charge storage performance, while the introduction of $NH_4^+$ into $V_2O_5$ ($NH_4$-$V_2O_5$) not only increases the interlayer distance ($d_{(001)}$ = 15.99 Å), but also significantly increases the $V^{4+}/V^{5+}$ redox couple (atomic concentration ratio increased from 0.14 to 1.08), resulting in the highest electrochemical performance. The $NH_4$-$V_2O_5$ cathode exhibited a high specific capacity (310.8 mAh $g^{-1}$ at 100 mA $g^{-1}$), improved cycling stability, and a significantly reduced charge transfer resistance (~ 17.9 Ω) compared to pristine $V_2O_5$ (112.5 mAh $g^{-1}$ at 0.1A $g^{-1}$ and ~ 65.58 Ω charge transfer resistance). This study enhances our understanding and contributes to the development of high-capacity cathode materials, offering valuable insights for the design and optimization of cathode materials to enhance the electrochemical performance of ZIBs.

**Keywords:** Pre-doped cations strategy, layered vanadium pentoxide, tuning oxidation states of vanadium, High-charge storage performance, zinc-ion batteries.

## Introduction

The increasing demand for efficient and sustainable energy storage systems has been driven by the rising adoption of renewable energy sources and the urgency to address global warming concerns. While lithium-ion batteries (LIBs) have dominated the market, their limitations such as limited lithium availability, safety issues, and restricted energy density have spurred interest in exploring alternative battery systems.[1-4] Aqueous rechargeable zinc-ion batteries (ZIBs) have emerged as promising candidates due to their abundance, cost-effectiveness, and environmental friendliness. Moreover, their compatibility with aqueous electrolytes offers inherent safety advantages over the flammable organic electrolytes used in traditional LIBs. However, the development of high-performance cathode materials for ZIBs remains a challenging task. Extensive research has focused on manganese oxide,[5] Prussian blue analogs,[6] vanadium oxide materials,[7] and organic compounds.[8] Vanadium oxide-based materials have garnered significant attention due to their high theoretical capacity, multiple oxidation states, and layered structure that facilitates the storage of zinc ions. However, the progress in vanadium cathode development has been impeded by slow ion diffusion, and unstable cycling performance. To address these issues, defect engineering, cation doping, and other approaches have been employed to enhance battery performance.[7, 9] For example, Guo et al. fabricated a layered $K_{0.5}V_2O_5$ with an increased interlayer distance of 9.51 Å, resulting in a boosted capacity of approximately 90 mAh $g^{-1}$ at 10 mA $g^{-1}$.[10] Xu et al. introduced $Mg^{2+}$ doping in $V_2O_5$, broadening the interlayer distance to 10.76 Å and achieving significantly improved cycling stability with 86.9% capacity retention after 500 cycles.[11] Zheng et al. synthesized $Al^{3+}$ doped hydrated vanadate, attaining a high capacity of 380 mAh $g^{-1}$ at 50 mA $g^{-1}$ and maintaining long-term cycling capacity over 3000 cycles.[12]

Based on these findings, it is evident that doping cations not only contribute to the stabilization of the crystal structure during cycling but also play a crucial role in enlarging the interlayer distance, thereby improving the overall capacity. However, the specific functions of different cations in this regard have not been extensively studied. Therefore, the objective of this study was to synthesize and evaluate four types of materials: pristine vanadium oxide ($V_2O_5$), sodium-doped vanadium oxide (Na-$V_2O_5$), potassium-doped vanadium oxide (K-$V_2O_5$), and ammonium-doped vanadium oxide ($NH_4$-$V_2O_5$). Through an analysis of their electrochemical performance, it was observed that $NH_4$-$V_2O_5$ exhibited superior performance compared to the other compositions. Notably, the creation of $V^{4+/}V^{5+}$ redox couples, particularly through an increase in the presence of $V^{4+}$, significantly enhanced the electrochemical performance. These

findings provide valuable insights for the future design and development of high-performance cathode materials.

**Results and Discussion**

The samples were prepared using chemical routes (see Experimental section) and subsequently processed in hydrothermal reactors. After preparation, their morphology was analyzed using scanning electron microscopy (SEM) and transmission electron microscopy (TEM). **Figure 1a** shows that the pristine $V_2O_5$ sample has a nanofiber structure with diameters ranging from 20 nm to 100 nm. The interplanar spacing of 2.208 Å corresponds to the (311) plane according to the reference PDF 03-065-0131 (**Figure 1b, c**). This observation is supported by the selected area electron diffraction (SAED) results shown in **Figure S1a**. The dots in the SAED pattern correspond to the crystalline planes (201), (301), and (111), with corresponding d-spacings of 3.478 Å, 2.925 Å, and 2.673 Å, respectively. On the other hand, the $NH_4$-$V_2O_5$ sample exhibits a nanoflakes structure based on the SEM image (**Figure 1d**). The d-spacing calculated from a specific point in the high-resolution TEM (HRTEM) image (**Figure 1e**) is found to be 2.003 Å, which corresponds to the X-ray diffraction (XRD) pattern from PDF 01-078-2016. The SAED (**Figure S1b**) analysis further confirms the presence of specific planes, namely (0 -2 1), (0 -3 3), and (2 -1 4), with corresponding d-spacings of 6.618 Å, 3.598 Å, and 3.261 Å, respectively. The morphologies of Na-$V_2O_5$ and K-$V_2O_5$ are not described in the given text but are shown in **Figure S2** and **S3**. The energy-dispersive X-ray spectroscopy (EDS) images suggest that the cations are uniformly doped in the materials (see **Figure S4**). The XRD patterns of the samples correspond to the crystal structures of $V_2O_5$ (orthorhombic crystal structure with space group Pmmn (59)), $NH_4$-$V_2O_5$ (anorthic crystal structure with space group P-1), Na-$V_2O_5$ (orthorhombic crystal structure with space group Pnma (62)), and K-$V_2O_5$ (monoclinic crystal structure with space group C12). These XRD patterns are consistent with the SAED and HRTEM patterns ($V_2O_5$: a = 11.5120 Å, b = 3.5640 Å, c = 4.3680 Å; $NH_4$-$V_2O_5$: a = 13.1730 Å, b = 14.3310 Å, c = 16.0230 Å; K-$V_2O_5$: a = 11.6570 Å, b = 3.6590 Å, c = 9.4600 Å and Na-$V_2O_5$: a = 9.3620 Å, b = 3.6080 Å, c = 22.0580 Å). To further investigate the optical properties of the samples, the UV-Vis absorption spectrum is explored and presented in **Figure 1h**. It is observed that there are significant change in the optical absorption properties among the samples. The calculated optical bandgap energies for $V_2O_5$, $NH_4$-$V_2O_5$, Na-$V_2O_5$, and K-$V_2O_5$ samples are ~ 2.5 eV, ~ 2.3 eV, ~ 2.4 eV, and ~ 2.0 eV, respectively (see **Figure S5**). Moreover, **Figure 1i s**hows Raman spectra that exhibit characteristic shifts that can be assigned as follows the peak centered around ~ 993 $cm^{-1}$ corresponds to the stretching vibration of the vanadyl

bond (V=O). The peak at ~ 700 $cm^{-1}$ is associated with the stretching of V-O-V bonds. The peak located at ~526 $cm^{-1}$ corresponds to the $V_3O$ phonon band. The peak at ~ 404 $cm^{-1}$ represents the angle-bending vibration of V-$O_{(3)}$-V. The peak at ~304 $cm^{-1}$ corresponds to the bending vibration of V-$O_C$. The peak at ~284 $cm^{-1}$ corresponds to the bond bending vibration of $O_C$-V-$O_B$. The peak at ~197 $cm^{-1}$ represents the bending vibration of $O_C$-V-$O_B$ ($A_g$ mode) bond. Finally, the peak at ~145 $cm^{-1}$ corresponds to the vibration mode of V-O-V chains.[13] For $NH_4$-$V_2O_5$, the peaks centered around ~ 142 and ~ 283 $cm^{-1}$ are assigned to the bending vibration of O-V=O. The peaks at ~194, ~301, and ~ 405, and 476 $cm^{-1}$ are attributed to the bending vibration of V-O-V. The peaks at ~692 $cm^{-1}$ is associated to the stretching vibration of the V-O bond.[14] The peak at ~993 $cm^{-1}$ is ascribed to the symmetric stretching vibration of V=O. For Na-$V_2O_5$, the peak at ~137 $cm^{-1}$ is assigned to the vibration mode of V-O-V chains with a blueshift. The peak at at ~ 200 $cm^{-1}$ is associated with the bending vibration with a red shift. The peak ~ 692 $cm^{-1}$ mode corresponds to the antisymmetric stretching of $V_{(1)}$–$O_{(2)}$–$V_{(1)}$ and the mode at ~1014 $cm^{-1}$ represents the $V_{(2)}$–$O_{(6)}$ stretching vibration.[15] For K-$V_2O_5$, the characteristic peak ~1014 $cm^{-1}$ is ascribed to the V=O stretching modes in the δ-phase. The peaks at ~500 and ~ 686 $cm^{-1}$ are assigned to the stretching modes of the V-O bonds. The peaks at 416 $cm^{-1}$ is correspond to the V=O bending vibration.[16]

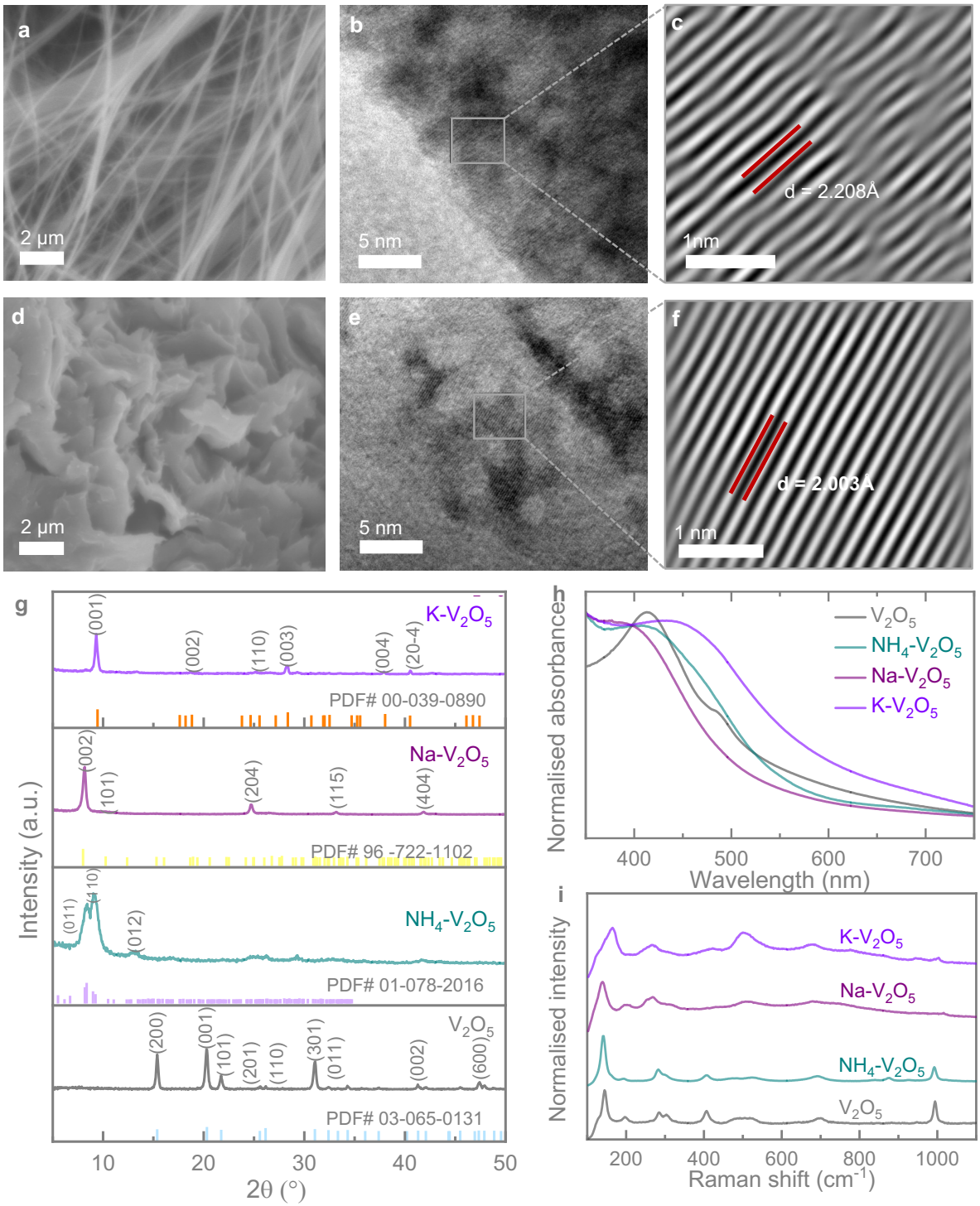


***Figure 1.*** *SEM and HRTEM images of $V_2O_5$ (a-c) and $NH_4$-$V_2O_5$ (d-f). (g-i) XRD, UV-Vis and Raman spectra of the $V_2O_5$, $NH_4$-$V_2O_5$, Na-$V_2O_5$ and K-$V_2O_5$.*

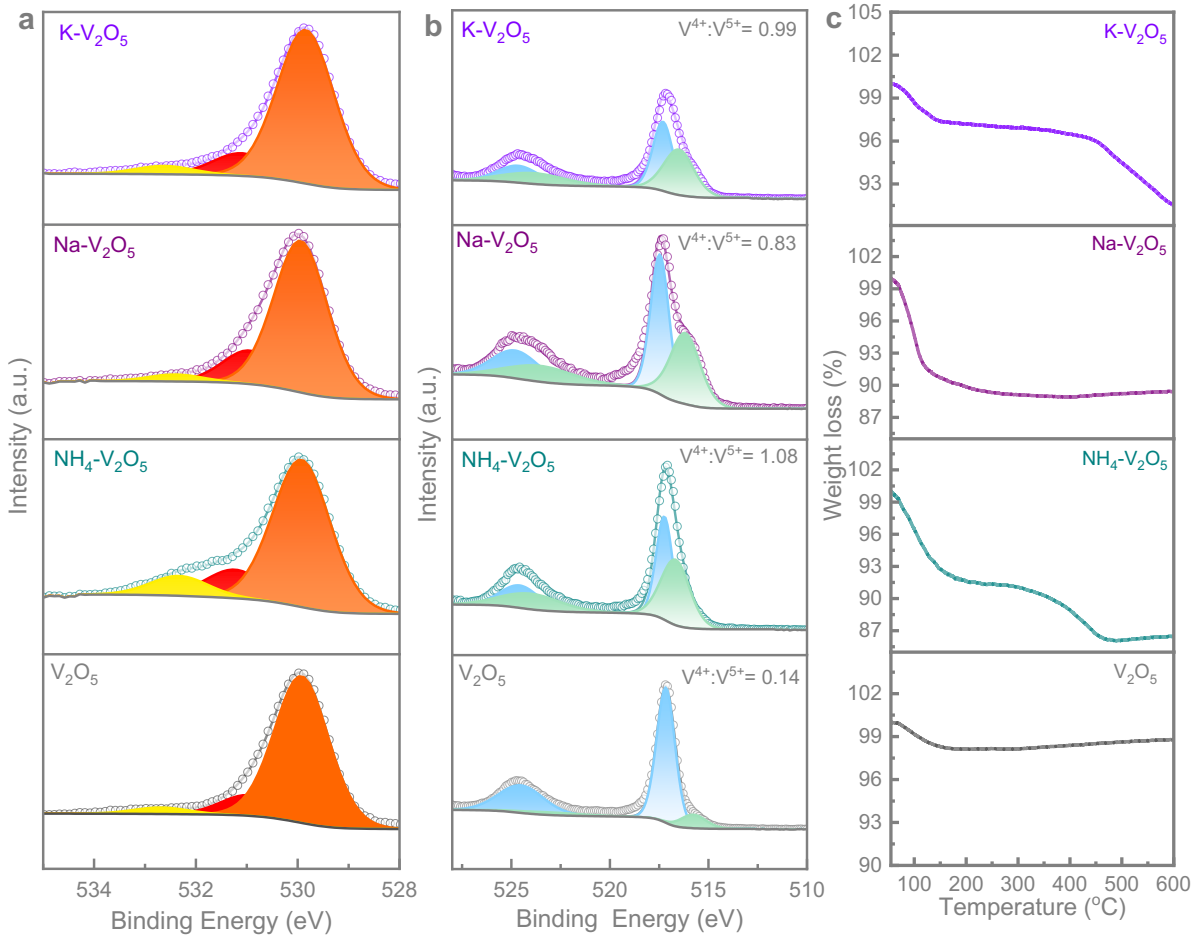


***Figure 2.*** *XPS spectra of the samples: (a) O1s and (b) V2p1/2 and V2p3/2. (c) TGA curves of the of the samples.*

To gain a better understanding of the formulation and oxidation states of vanadium in the samples, we conducted an X-ray photoelectron spectroscopy (XPS) investigation. In **Figure 2a**, the O 1s spectrum appears broad and asymmetric, allowing for its deconvolution into three peaks. These peaks indicate the presence of three different oxygen species. The peaks are located at approximately ~ 529.95 eV (fitted orange peak), ~ 531.00 eV (fitted red peak), and ~532.40 eV (fitted yellow peak). The peaks correspond to which correspond to the lattice oxygen $O^{2-}$, the absorbed $H_2O$ molecules and, oxygen vacancy, respectively.[17] Notably, the peaks related to the presence of $H_2O$ molecules and oxygen vacancy exhibit a noticeable increase in intensity in $NH_4$-$V_2O_5$ compared to $V_2O_5$, following the order : absorbed $H_2O$ molecules Na-$V_2O_5$ (10.25%) > $NH_4$-$V_2O_5$ (9.13%) > K-$V_2O_5$ (7.5%) > $V_2O_5$ (7.07%); oxygen vacancy from $NH_4$-$V_2O_5$ (6.31%) > K-$V_2O_5$ (2.76%) > $V_2O_5$ (2.24%) > Na-$V_2O_5$ (2.14%). **Figure 2b** illustrates the core level binding energies of the V 2p3/2 and V 2p1/2 spectra, which can be divided into four peaks at approximately ~ 517.16 eV and 524.51 eV (fitted light blue)

peaks attributed due to the presence of pentavalent state ($V^{5+}$), whereas ~ 523.10 eV and ~ 515.76 eV (fitted light green) which correspond to the tetravalent vanadium ($V^{4+}$). The ratio of $V^{4+}$:$V^{5+}$ increases in the doped samples, following the order $NH_4$-$V_2O_5$ (1.08) > K-$V_2O_5$ (0.99) > Na-$V_2O_5$ (0.83) > $V_2O_5$ (0.14) (**Figure S1**). This indicates an increase in the presence of $V^{4+}$ after doping compared to the pristine $V_2O_5$ sample. Among the doped samples, $NH_4$-$V_2O_5$ exhibits the highest value of $V^{4+}$. **Figure 2c** presents the thermogravimetric analysis (TGA) curves of the samples. The weight losses of 1.87% ($V_2O_5$), 8.41% ($NH_4$-$V_2O_5$), 10.16% (Na-$V_2O_5$), and 2.80% (K-$V_2O_5$) observed in the temperature range of 55-200 °C are attributed to the removal of adsorbed and constitutional water molecules. The order of water molecule content, as indicated in **Figure 2a**, aligns with the XPS results.

Next, the electrochemical performance of the electrodes was thoroughly investigated against a zinc (Zn) anode by assembling coin cells according to the experimental procedure outlined in the experimental section. To assess the performance, the first cyclic voltammogram (CV) was conducted across a range of scan rates from 0.2 to 1.0 mV $s^{-1}$, covering a potential window of 0.2 to 1.6 V. **Figure 3a** depicts the CVs of the $V_2O_5$ electrode, showcasing distinct pairs of oxidation and reduction peaks. These peaks are observed around specific voltage values, such as major peaks (~ 1.2 V / ~ 0.9 V) and minor peaks (~ 0.7V / ~ 0.5V), which are attributed to the intercalation and de-intercalation processes of $Zn^{2+}$ ions.[18,19] The CVs of $NH_4$-$V_2O_5$, on the other hand, exhibit pronounced oxidation and reduction peaks with significantly higher specific peak currents when compared to pristine $V_2O_5$. This enhanced performance suggests an improved capability for charge storage in $NH_4$-$V_2O_5$. For a comprehensive analysis, the CVs of Na-$V_2O_5$ and K-$V_2O_5$ can be found in the Supporting Information (**Figures S6 and S7**). It is noteworthy that all the doped electrodes display enhanced charge storage capabilities compared to the pristine $V_2O_5$ electrodes. Notably, $NH_4$-$V_2O_5$ electrodes demonstrate the highest response among the doped samples. Furthermore, when comparing the CVs at 0.5 mV $s^{-1}$ and 1.0 mV $s^{-1}$, it becomes evident that the redox peak currents are substantially improved, indicating a significant enhancement in charge storage activities across the doped electrodes. Overall, these findings highlight the superior electrochemical performance of the doped electrodes, with $NH_4$-$V_2O_5$ exhibiting the most notable improvements.

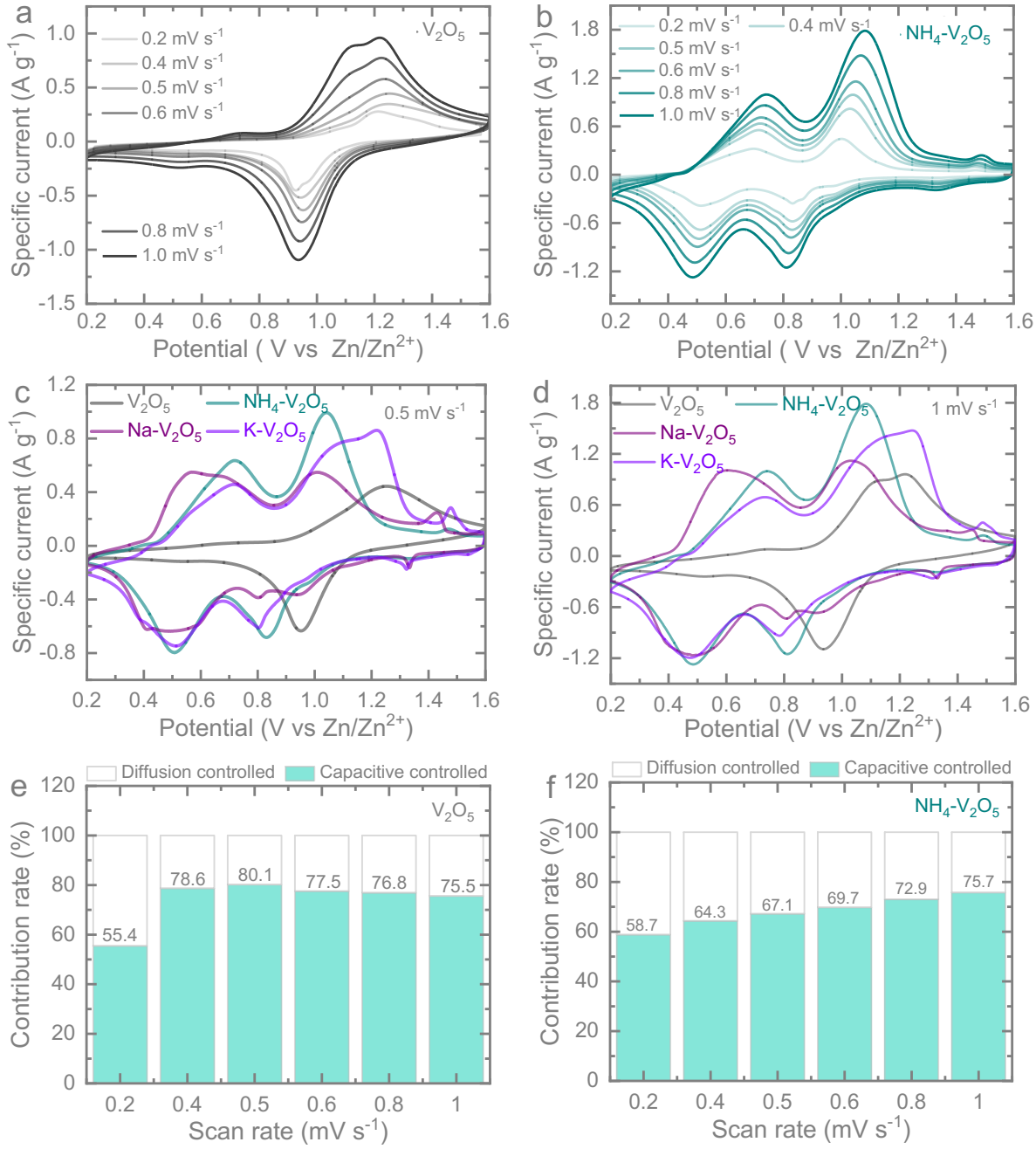


***Figure 3.*** *CV curves of (a) $V_2O_5$ and (b) $NH_4$-$V_2O_5$ obtained at various scan rates ranging from 0.2 to 1.0 mV $s^{-1}$ within a voltage window of 0.2 to 1.6 V. Comparison of the CVs of the samples at scan rates of (c) 0.5 mV $s^{-1}$ and (d) 1.0 mV $s^{-1}$. Estimation of the charge storage contribution for (e) $V_2O_5$ and (f) $NH_4$-$V_2O_5$ electrodes.*

To analyze the charge storage process, we can break it down into two components: capacitive-controlled ($k_1 v$) and diffusion-controlled ($k_2 v^{1/2}$). This relationship can be represented by the current at a fixed voltage equation: $i(V) = k_1 v + k_2 v^{1/2}$ .[20,21] Using this equation, we

calculated the capacitive contribution, as shown in **Figures 3e, 3f, S6b** and **S7b**, for different electrodes. At a scan rate of 0.2 mV $s^{-1}$, the estimated capacitive contributions for $V_2O_5$, $NH_4$-$V_2O_5$, Na-$V_2O_5$, and K-$V_2O_5$ electrodes were 55.40%, 58.7%, 65%, and 39.7%, respectively. These values increased to 75.5%, 75.7%, 80.5%, and 59.4% when tested at 1.0 mV $s^{-1}$. A higher capacitive profile indicates a better ability to operate batteries at high rates. Therefore, among all the electrodes, $NH_4$-$V_2O_5$ and Na-$V_2O_5$ electrodes appear to be more suitable for high-rate operation (see further). Furthermore, $NH_4$-$V_2O_5$ demonstrates superior charge storage performance even at lower rates (for more information, please see the accompanying details).

The charge storage analysis of the electrodes was further extended by evaluating the galvanostatic discharge-charge (GDC) response at different specific currents, ranging from 100 mA $g^{-1}$ to 5000 mA $g^{-1}$, across the working potential range of 0.2 V to 1.6 V. Detailed GDC curves for $V_2O_5$ and $NH_4$-$V_2O_5$ at various specific currents are shown in **Figures 4a** and **b**, respectively. Consistent with the CV results, $NH_4$-$V_2O_5$ demonstrated higher specific capacities compared to the other electrodes. For example, at a specific current of 100 mA $g^{-1}$, the observed specific capacities (2$^{nd}$ cycle) were 99.6 mAh/g, 302.4 mAh/g, 238.17 mAh/g, and 276 mAh/g for $V_2O_5$, $NH_4$-$V_2O_5$, Na-$V_2O_5$, and K-$V_2O_5$ electrodes, respectively. **Figures 4c** and **d** clearly illustrate the capacity improvements in the doped samples compared to pristine $V_2O_5$. However, at a high specific current of 5000 mA $g^{-1}$, the specific capacities of $NH_4$-$V_2O_5$ and Na-$V_2O_5$ were nearly equal (159 mAh $g^{-1}$). This similarity could be attributed to the higher capacitive-controlled charge storage contribution, which dominates at relatively higher rates. Supplementary Information **Figure S8** provides additional GDC curves for Na-$V_2O_5$ and K-$V_2O_5$ electrodes. The observed capacity improvements in the electrodes closely follow the presence of $V^{4+}$:$V^{5+}$ states (**Figure 2b, Table S1)**, following the sequence $V_2O_5$ < Na-$V_2O_5$ < K-$V_2O_5$ < $NH_4$-$V_2O_5$. This sequential order directly corresponds to the charge storage performance. Therefore, the highest capacity observed in $NH_4$-$V_2O_5$ compared to the other electrodes can primarily be attributed to the higher concentration of $V^{4+}$, which is more efficient for reversible $Zn^{2+}$ storage.[22-24]

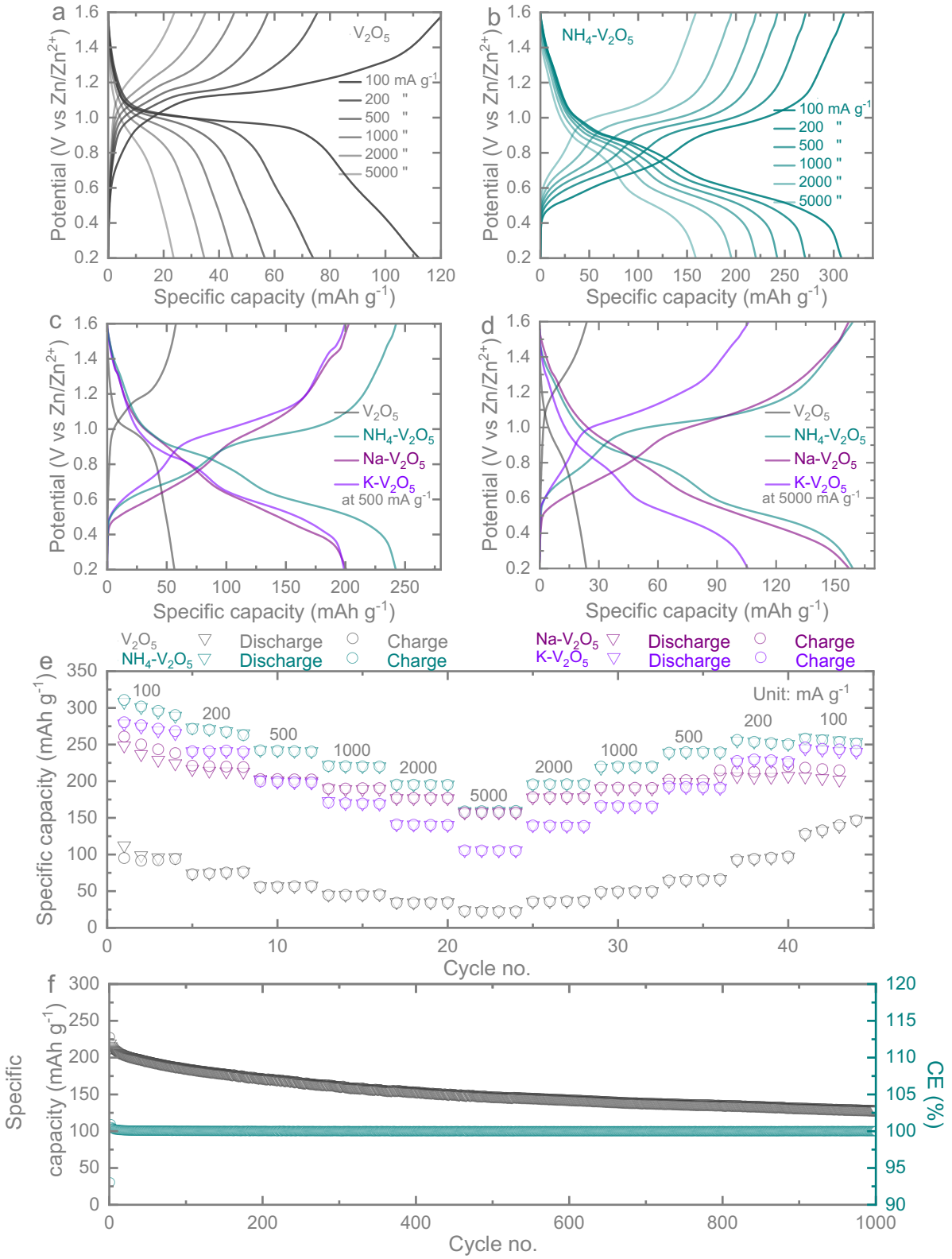


***Figure 4.*** *(a, b) GDC curves of $V_2O_5$ and $NH_4$-$V_2O_5$ at various specific currents, spanning from 100 mA $g^{-1}$ to 5000 mA $g^{-1}$, across the voltage range of 0.2 V to 1.4 V. (c, d) Comparative GDC curves of the electrodes at specific currents of 500 mA $g^{-1}$ and 5000 mA $g^{-1}$, respectively. (e)*

*Rate tests showcasing the performance of the electrodes. (f) Long-term cycling test of $NH_4$-$V_2O_5$, where CE represents coulombic efficiency in the plot.*

In addition to GDC tests, electrochemical impedance spectroscopy (EIS) tests were conducted within a frequency range of 10 mHz to 100 kHz with a voltage amplitude of 10 mV. These tests were performed after the 2nd GDC cycle to 0.7 V. The Nyquist plots in **Figure S9** revealed the charge transfer resistances of the cells, which were measured to be approximately 65.58 Ω for $V_2O_5$, 17.9 Ω for $NH_4$-$V_2O_5$, 19.78 Ω for Na-$V_2O_5$, and 10.66 Ω for K-$V_2O_5$ cells. These results further confirm that the doped samples exhibit better charge storage kinetics compared to the pristine counterpart. Furthermore, long-term cycling tests at 1000 mA $g^{-1}$ for 1000 cycles were conducted, as depicted in **Figures 4a** for $NH_4$-$V_2O_5$, a capacity retention of approximately 60.58% and a coulombic efficiency (CE) of 100% were achieved after 1000 cycles.

In conclusion, this study focused on the investigation of pre-doping of various cations, including $Na^+$, $K^+$ and $NH_4^+$ into $V_2O_5$ to enhance the overall charge storage performance of ZIBs. Our findings highlight the crucial role played by $V^{4+}$ species in enhancing the cathode material's charge storage performance. Additionally, the introduction of $NH_4^+$ into $V_2O_5$, resulting in $NH_4$-$V_2O_5$, led to notable improvements. One significant improvement observed was the increase in interlayer distance to 15.99 Å ($d_{(001)}$ = 15.99 Å), which promotes efficient diffusion of Zn ions within the material. Moreover, the reduction of the $V^{4+}/V^{5+}$ redox couple ratio from 0.14 to 1.08 demonstrates enhanced electrochemical performance. The $NH_4$-$V_2O_5$ cathode exhibited a high specific capacity of 310.8 mAh $g^{-1}$ at 100 mA $g^{-1}$, indicating its ability to store a substantial amount of charge with improved cycling stability. By advancing our understanding of the doping process and the role of different cations in $V_2O_5$, this study provides valuable insights for the design and optimization of cathode materials in ZIBs. These insights contribute to the ongoing efforts to develop more efficient and reliable rechargeable battery systems, ultimately enhancing the charge storage performance and overall sustainability of ZIB technology.

**Experimental Section**

*Chemicals:* All chemicals in the study were of analytical grade and used directly without any further purification. Vanadium pentoxide, hydrogen peroxide solution 30% (w/w), ammounium metavanadate, potassium iodide, polyethylene glycol (Mw 4000), sulfuric acid (95-97%), $Zn(CF_3SO_3)_2$, ethanol and poly(vinyl difluoride) were received from Sigma-Aldrich. N-

Methyl-2-pyrrolidone technical was purchased from VWR international. Sodium hydroxide pellets, 98% was purchased from thermo scientific. Potassium chloride was received from EMSURE®. Reduced graphene oxide powder (rGO), P3HT (Mw=60,150 97.6% RR) were purchased from Ossila.

*Material synthesis:* Pristine $V_2O_5$ was synthesized using a hydrothermal process. In this process, 1.0930 g of $V_2O_5$ powder was added to 90 mL of deionized (DI) water , and the solution was vigorously stirred at around 300 rpm for 30 minutes at room temperature. Following that, 15 mL of 30% $H_2O_2$ was added to the solution, and stirring continued for an additional 30 minutes. The resulting transparent orange solution was then transferred into a 150 mL autoclave and placed in an oven at 205 °C for 3 days. Once cooled to room temperature, the products were washed alternately with DI water and ethanol and finally dried in a vacuum oven overnight at 70 °C.

The synthesis of $NH_4$-$V_2O_5$ was conducted following the method described in ref. 25. In this procedure, 1.755 g of ammonium metavanadate was added to 90 mL of DI water. The solution was stirred for 30 minutes before adding 0.9 mL of $H_2SO_4$ to the suspension. Stirring was continued for an additional 30 minutes. The resulting suspension was then transferred to a 150 mL autoclave and placed in an oven at 100 °C for 2 days. After cooling to room temperature, the products were washed alternately with DI water and ethanol and dried in a vacuum oven overnight at 70 °C.

The synthesis of Na-$V_2O_5$ followed the method described in ref. 26. Initially, 0.3636 g of pristine $V_2O_5$ was dissolved in a mixture of 60 mL of DI water and 0.7 mL of NaOH solution (1 mol/L). The solution was sonicated at room temperature for 1 hour. Subsequently, 0.2 g of Polyethylene glycol (MW 4000) was added to the solution, and stirring was continued for another 15 minutes. The solution was then transferred to a 150 mL autoclave and placed in an oven at 180 °C for 2 days. After cooling to room temperature, the products were washed alternately with DI water and ethanol and dried in a vacuum oven overnight at 70 °C.

The fabrication of K-$V_2O_5$ followed the procedure described in ref. 10. In this process, 0.5456 g of pristine VO, 0.747 g of KI, and 6.709 g of KCl were dissolved in 90 mL of DI water with magnetic stirring for 30 minutes. The solution was transferred to a 150 mL autoclave and placed in an oven at 200 °C for 1 day. After cooling to room temperature, the products were washed alternately with DI water and ethanol and dried in a vacuum oven overnight at 70°C.

*Characterization:* The obtained materials underwent characterization using various analytical methods. SEM analysis was conducted using a Zeiss EVO LS15, Oxford Instruments X-MaxN,

and Hitachi TMA4000Plus. TEM, EDS, and SAED were performed using a JEOL JEM-2100 TEM operated at 200 kV. XRD patterns of the samples were obtained using the Panalytical Empyrean XRD instrument with Cu Kα radiation. The measurements were conducted at 40 kV and 40 mA, with a step size of 0.05° and a scanning rate of 0.1° $s^{-1}$, covering a 2θ range from 2° to 70°. UV-Vis analysis was carried out using the PerkinElmer Lambda 750S instrument. Raman spectroscopy was performed using the Renishaw inViaTM confocal Raman microscope with a laser wavelength of 515 nm. XPS analysis was conducted using the ThermoFisher Scientific XPS instrument. The XPS data were acquired using monochromatic Al $K_\alpha$ X-rays (1486.6 eV), with a pass energy of 50 and 200 eV for narrow and wide spectra, respectively. No significant sample charging was observed, and charge referencing was done against adventitious carbon (C 1s, 284.8 eV). The spectra are presented with intensity in counts per second (CPS), and the experimental peaks were fitted using CasaXPS software.

*Preparation of cathodes and coin-cells:* To prepare the cathodes, 80 mg of active material, consisting of either $V_2O_5$ , $NH_4$-$V_2O_5$, Na-$V_2O_5$, or K-$V_2O_5$ , along with 10 mg of rGO and 5 mg of P3HT, was dispersed in 2 mL of NMP through a sonication process. Subsequently, 5 mg of PVDF (polyvinylidene fluoride) was added to the solution. The resulting electrode solution was drop-cast onto CF (Sigracet GDL 39 AA carbon graphite paper, SGL Carbon) current collectors and dried under vacuum conditions at 70°C, resulting in the formation of the cathodes. The CR 2032 coin-cells were assembled by placing a titanium foil on the coin-cell case, followed by the placement of a cathode disc. A Whatman glass microfiber filter paper was then placed as a separator. Next, 150 μL of a 3M $Zn(CF_3SO_3)_2$ aqueous electrolyte was added to the cell, and finally, a Zn counter electrode was introduced in sequence.

*Electrochemical Tests:* CV measurements were carried out using a Biologic VMP-3 galvanostat, covering a potential window of 0.2 V to 1.6 V after resting the cells for 10 hours. The measurements were conducted at various scan rates ranging from 0.2 to 1.0 mV/s. GDC measurements were performed over the same potential window at different specific currents, ranging from 100 to 5000 mA $g^{-1}$. The cycling performance of the electrodes was evaluated by testing them using Neware (BTS4000) at a constant current of 1000 mA $g^{-1}$ for 1000 cycles, maintaining the same potential window. EIS tests (Autolab, PGSTAT302N) were conducted within a frequency range of 10 mHz to 100 kHz, using a voltage amplitude of 10 mV.

## ASSOCIATED CONTENT

Supporting Information

The Supporting Information is available

SAED patterns (Figure S1); SEM, TEM, HRTEM images and SAED patterns (Figures S2, S3); Computed $V^{4+}$ and $V^{5+}$ values (Table S1); EDS mappings (Figure S4); Tauc plots (Figure S5); CVs and estimation of the charge storage contribution (Figures S6, S7); GCDs of Na-$V_2O_5$ and K-$V_2O_5$ (Figure S8); Nyquist plots and equivalent circuit model (Figure S9).

AUTHOR INFORMATION

*Corresponding Authors:

Prof. Ivan P. Parkin – i.p.parkin@ucl.ac.uk

Dr. Buddha Deka Boruah – b.boruah@ucl.ac.uk

Notes

The authors declare no competing financial interest.

**Acknowledgements**

**Reference**

1. N. Mahmood, T. Tang, Y. Hou, *Adv. Energy Mater.* **2016**, *6*, 1600374.

2. S. Passerini, B. Scrosati, *Electrochemical Society Interface* **2016**, *25*, 85–87.

3. Q. Huang, S. Ni, M. Jiao, X. Zhong, G. Zhou, H. M. Cheng, *Small* **2021**, *17*, 2007676.

4. B. Diouf, R. Pode, *Renewable Energy* **2015**, *76*, 375–380.

5. Q. Chen, J. Jin, Z. Kou, C. Liao, Z. Liu, L. Zhou, J. Wang, L. Mai, *Small* **2020**, *16*, 2000091.

6. L. Zhang, L. Chen, X. Zhou, Z. Liu, *Adv. Energy Mater.* **2015**, *5*, 1400930.

7. H. Chen, S. Cheng, D. Chen, Y. Jiang, E. H. Ang, W. Liu, Y. Feng, X. Rui, Y. Yu, *Materials Chemistry Frontiers* **2021**, *5*, 1585-1609.

8. C. Han, H. Li, R. Shi, T. Zhang, J. Tong, J. Li, B. Li, *J. Mater. Chem. A* **2019**, *7*, 23378-23415.

9. K. Zhu, S. Wei, H. Shou, F. Shen, S. Chen, P. Zhang, C. Wang, Y. Cao, X. Guo, M. Luo, H. Zhang, *Nat. Commun.* **2021**, *12*, 6878.

10. L. Deng, X. Niu, G. Ma, Z. Yang, L. Zeng, Y. Zhu, L. Guo, *Adv. Funct. Mater.* **2018**, *28*, 1800670.

11. X. Xu, M. Duan, Y. Yue, Q. Li, X. Zhang, L. Wu, P. Wu, B. Song, L. Mai, *ACS Energy Lett.* **2019**, *4*, 1328-1335.

12. J. Zheng, C. Liu, M. Tian, X. Jia, E. P. Jahrman, G. T. Seidler, S. Zhang, Y. Liu, Y. Zhang, C. Meng, G. Cao, *Nano Energy* **2020**, *70*, 104519.

13. D. B. Boruah, B. Wen, M. D. Volder, *Nano Lett.* **2021**, *21*, 3527.

14. L. Xu, Y. Zhang, J. Zheng, H. Jiang, T. Hu, C. Meng, *Mater. Today Energy* **2020**, *18*, 100509.

15. P. He, G. Zhang, X. Liao, M. Yan, X. Xu, Q. An, J. Liu, L. Mai, *Adv. Energy Mater.* **2018**, *8*, 1702463.

16. L. Deng, X. Niu, G. Ma, Z. Yang, L. Zeng, Y. Zhu, L. Guo, *Adv. Funct. Mater.* **2018**, *28*, 1800670.

17. D. Wu, Y. Zhuang, F. Wang, et al. *Nano Res.* **2023**, *16*, 4880–4887.

18. B. D. Boruah, A. Mathieson, B. Wen, S. Feldmann, W. M. Dose, M. D. Volder, *Energy Environ. Sci.* **2020**, *13*, 2414-2421.

19. Y. Li, Z. Huang, P. K. Kalambate, et al. *Nano Energy* **2019**, *60*, 752–759

20. B. D. Boruah, A. Mathieson, S. K. Park, et al.; *Adv. Energy Mater.* **2021**, *11*, 2100115.

21. B. D. Boruah, B. Wen, M. D. Volder, *ACS Nano* **2021**, *15*, 16616–16624.

22. F. Liu, Z. Chen, G. Fang, et al. *Nano-Micro Lett.* **2019**, *11*, 25.

23. H. Chen, J. Huang, S. Tian, et al. *Adv. Sci.* **2021**, *8*, 2004924.

24. M. Tian, C. Liu, J. Zheng, et al. *Energy Storage Mater.* **2020**, *29*, 9-16.

25. L. Xu, Y. Zhang, J. Zheng, H. Jiang, T. Hu, C. Meng, *Mater Today Energy* **2020**, *18*, 100509.

26. P. He, G. Zhang, X. Liao, M. Yan, X. Xu, Q. An, J. Liu, L. Mai, *Adv. Energy Mater.* **2018**, *8*, 1702463.